PAPER

Check for updates

Spontaneous structural deformation of MoS$_2$ nanoribbons in Au(111)/MoS$_2$/Au(111) heterojunctions

Xinghui Tang,[a] Hao Wang,[a] Kah Meng Yam, [ID][ab] Jiulin Tang,[a] Yongjie Zhang,[ac] Na Guo[d] and Chun Zhang [ID] *[ae]

Using first-principles simulations, we demonstrate that MoS$_2$ nanoribbons adsorbed between two Au(111) electrodes in an Au/MoS$_2$/Au junction undergo spontaneous structural deformation involving bending and stretching. This deformation increases the mechanical strain energy within the nanoribbon but is energetically compensated by enhanced adsorption on the Au electrodes, owing to the larger contact areas formed in the deformed configuration. The influence of these spontaneous structural deformations on the electronic and transport properties of the junction is investigated using state-of-the-art first-principles methods. Our results reveal that deformation lowers the energies of conduction bands associated with edge states, leading to a pronounced narrowing of the bandgap in the deformed nanoribbons. For narrow nanoribbons with widths around 1.5 nm, this deformation markedly enhances the junction's conductivity by facilitating electron tunneling through the conducting localized edge states.

1. Introduction

Two-dimensional (2D) materials have been regarded as one of the most promising candidates for next-generation electronic materials.[1–4] Among them, molybdenum disulfide (MoS$_2$) has emerged as a leading contender for advancing electronic device technologies.[5–8] MoS$_2$ combines mechanical flexibility, electronic tunability, optical responsiveness, and chemical stability with a sizable direct band gap of $\sim$1.8 eV,[9–12] making it highly attractive for applications in field-effect transistors (FETs) and optoelectronic devices.[13–15]

It has been shown in the literature that the structure deformation in 2D MoS$_2$ could greatly impact the electronic and transport properties of MoS$_2$. Recent experiments[16,17] demonstrated that when MoS$_2$ is grown on engineered substrates, structure deformations such as wrinkled or crested surfaces can occur, which dramatically enhance its conductivity by up to two orders of magnitude. A set of earlier computational

studies showed that a particular type of structure deformation, the bending, could significantly modify the electronic structures of MoS$_2$ nanoribbons.[18–20] These studies were based on ideal artificial bending structures of MoS$_2$ nanoribbons. It was found that in general, the bandgap of a MoS$_2$ nanoribbon decreases when the curvature of the artificial bending structure increases.

In this work, by first-principles simulations, we show that MoS$_2$ nanoribbons adsorbed between two Au(111) electrodes in an Au/MoS$_2$/Au junction undergo spontaneous structural deformation involving bending and stretching. The deformation arises from the interplay between the mechanical energy accumulated in MoS$_2$ nanoribbon and the adsorption energy between Au electrodes and the MoS$_2$ nanoribbon. The spontaneous deformation is found to have intriguing effects on both electronic structures of the MoS$_2$ nanoribbon and transport properties of the Au/MoS$_2$/Au junction. These results could have important implications for future applications of MoS$_2$ based devices.

2. Computational details

Structure optimizations and band structure calculations were performed using the first-principles method based on density functional theory (DFT), as implemented in the Spanish initiative for electronic simulations with thousands of atoms

[a] *Department of Physics, National University of Singapore, 2 Science Drive 3, 117551, Singapore. E-mail: phyzc@nus.edu.sg*

[b] *Furen International School, 8 Claymore Hill 01-01, 229572, Singapore*

[c] *Department of Mechanical and Energy Engineering, Southern University of Science and Technology, Shenzhen, 518055, Guangdong, China*

[d] *College of Materials and Energy, Guangan Institute of Technology, No. 66, Ligong Avenue, Guangan 638000, Sichuan, China*

[e] *Department of Chemistry, National University of Singapore, 3 Science Drive 3, 117543, Singapore*

This journal is © The Royal Society of Chemistry 2026

J. Mater. Chem. C, 2026, **14**, 7641–7647 | 7641

(SIESTA) computational package.[21–23] The steady-state density functional theory (SS-DFT)[24,25] is used for transport calculations. The generalized gradient approximation (GGA) in the Perdew–Burke–Ernzerhof (PBE) format,[26] a double-ζ polarized basis set and the Troullier–Martins norm-conserving pseudopotentials[27] (with scalar-relativistic effects included for Au), were employed for all calculations. For structure and transport calculations, a $7 \times 1 \times 1$ k-point Monkhorst–Pack mesh in the Brillouin zone is used. For the density of states (DOS) calculations, a denser $13 \times 1 \times 1$ k-point grid is utilized to enhance accuracy. The electronic band structures of the isolated MoS_2 nanoribbon were calculated along the high-symmetry k-path Γ–X in the one-dimensional Brillouin zone. Convergence criteria for energy and force are set to 10^{-4} eV and 0.03 eV Å^{-1}, respectively. In SS-DFT calculations, nonequilibrium corrections for exchange energy functionals are considered.[28,29]

The DFT calculations with Vienna *Ab initio* Simulation Package (VASP)[30] were done to benchmark the band structures obtained from SIESTA. The VASP calculations used a plane-wave basis set with a kinetic energy cutoff of 450 eV, projector augmented-wave (PAW) pseudopotentials,[31] and the generalized gradient approximation (GGA) in the Perdew–Burke–Ernzerhof (PBE) form.

3. Results and discussion

3.1 Au(111)/MoS$_2$/Au(111) device model

The structure (top view and side view) of a MoS_2 nanoribbon is shown in Fig. 1a, where two edges are saturated with H atoms. The ribbon is periodic along the x direction. The width of the ribbon is defined by the number of Mo atoms in the z direction as shown in the side view of the ribbon. The calculated energy as a function of distance between a $N = 10$ MoS_2 nanoribbon

and Au(111) substrate is plotted in Fig. 1b (inset shows the structure), which suggests that 2.5 Å is the optimal binding distance. In the calculations, the structures of both the ribbon and Au surface are fixed. Because the electronic properties of MoS_2 are highly sensitive to strain,[32] the lattice constant of Au was uniformly compressed by approximately 3% to minimize the lattice mismatch between MoS_2 and the Au(111) surface. This small compression has been known to have a negligible influence on the electronic properties of Au.[33] In Fig. 1c, we show the initial structure (before the structure optimization) of the Au/MoS$_2$/Au device made of two Au(111) electrodes and a flat MoS_2 nanoribbon in middle. In the supercell shown in the figure, the structures of Au electrodes and the middle ribbon shown here are chosen to be optimized ones for isolated Au electrodes and the MoS_2 nanoribbon. The distance between Au electrodes and the middle ribbon is set to 2.5 Å. A 15 Å vacuum layer in y direction is added in the supercell to avoid interactions with adjacent cells. The following-up structure optimization of the supercell is done with DFT-based SIESTA package and will be discussed in the next session. The band structures of monolayer MoS_2 and the bulk Au obtained from SIESTA are almost identical with those calculated from the plane-wave based VASP package, as shown in SI Fig. S1a (monolayer MoS_2) and Fig. S1b (bulk Au), suggesting that the parameters we used for SIESTA calculations are reliable.

3.2 Spontaneous structure deformation of MoS$_2$ nanoribbons

During the structure optimization of the junction, three outermost layers on the left and right (enclosed parts in Fig. 1c) as well as the bottom layer of Au(111) are fixed, while all other atoms are allowed to move. Energy variation as a function of the iteration step during the optimization process is plotted in Fig. 2. The initial structure at step 0 is the same as that in
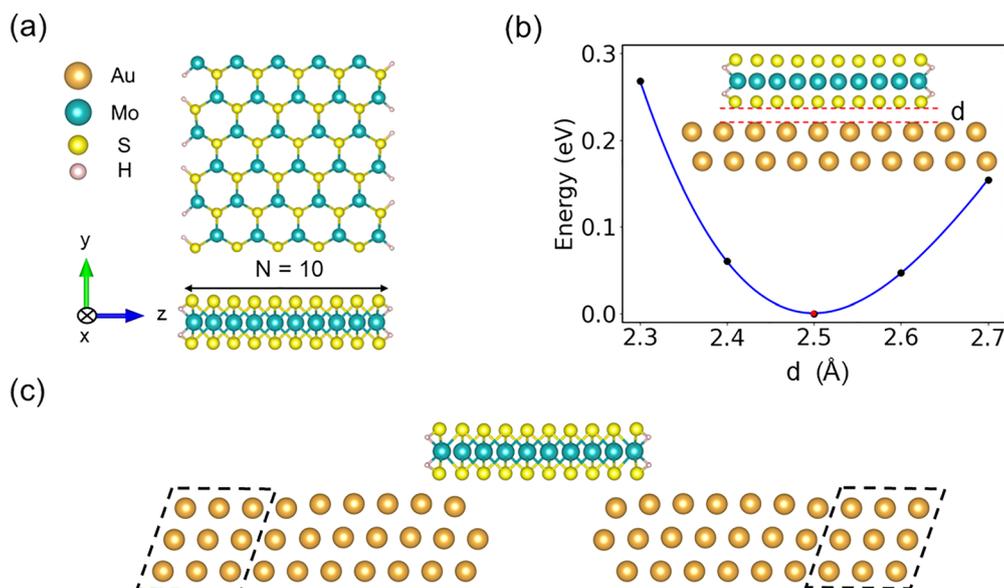

Fig. 1 (a) Top and side views of a MoS$_2$ nanoribbon with the width $N = 10$. (b) Calculated total energy as a function of the vertical distance (y direction) between the MoS$_2$ nanoribbon and the Au(111) substrate. (c) The initial structure of the Au/MoS$_2$/Au device.

Fig. 1(c), where the central ribbon with width $N = 10$ is flat. We see that during the optimization, the energy quickly drops, and the system finally ends up with a structure with a significantly deformed MoS_2 nanoribbon in the middle. The energy of the optimized structure is about 0.97 eV lower than the initial one with flat ribbon. The spontaneous structure deformation includes an obvious bending with a curvature around 0.03 $Å^{-1}$ (corresponding to a curvature radius around 32 Å) and a stretching in z direction around 0.12 Å. The definition of the curvature κ can be found in the inset of Fig. 2. Similar structure deformations are also observed for MoS_2 nanoribbons with different widths. In Table S1 (SI), we list the calculated curvature, curvature radius and the stretching of a few ribbons with the width ranging from $N = 10$ to $N = 18$.

The structure deformation is caused by the relatively strong interaction between the MoS_2 and the two Au electrodes. The deformation leads to higher energy of the ribbon due to the increased mechanical strain, while at the same time, the bending and stretching effectively increase the contact area between the ribbon and two electrodes, resulting in significantly stronger adsorption of the ribbon. Taking the $N = 10$ ribbon as an example, our calculations show that the energy of the isolated ribbon with structure deformation is about 0.48 eV higher than the flat one, while on two Au electrodes, the adsorption energy of the deformed ribbon is 0.97 eV stronger than that of the flat ribbon (Fig. 1c). The Bader charge analysis indicates that there are around 0.55 electrons transferred from Au electrodes to the deformed MoS_2, mainly in the contact region. As a comparison, for the structure with the flat ribbon (Fig. 1c), the charge transfer from Au electrodes to the ribbon is about 0.24 electrons.

We test the effects of van der Waals (vdW) interactions using the DFT+D3 correction[34] on the deformation of the ribbon. It is found that the vdW interactions cause a negligible increase of the curvature approximately 0.001 $Å^{-1}$. It is worth mentioning that whether an applied gate electric field[35] can be used to tune the structural deformation is a highly intriguing question, which we will address in future studies.
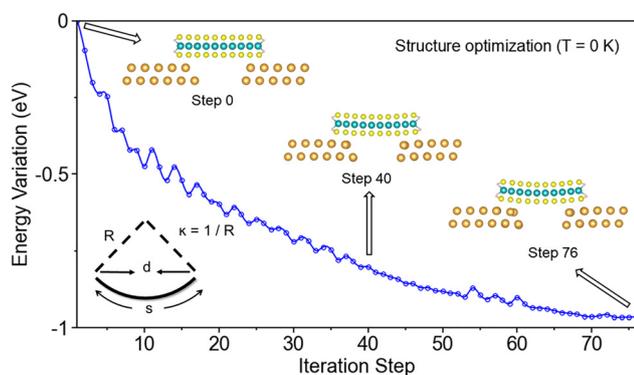
3.3 Deformation caused bandgap decrease

The structure deformation can have important effects on electronic structures of MoS_2 nanoribbons. In Fig. 4a, we plot band structures of both flat and deformed $N = 10$ ribbons, where C1, C2 and V1, V2 are two nearly degenerate conduction and valence bands, respectively. Two valence bands of the deformed ribbon remain almost the same as those of the flat one, while the deformation significantly brings down the energies of two conduction bands, resulting in a deformation-caused decrease of the band gap around 0.3 eV. Two conduction bands are localized edge states while two valence bands are more extending in nature, as clearly shown in iso-surface plots of wavefunctions (Fig. 4b). Apparently, the deformations (the bending and the stretching) significantly enhance the interactions between ions and localized electrons at edges (due to the weaker contributions from other ions), while having little effect on extending electron orbitals. To see this more clearly, we calculated the plane-averaged electrostatic potential along the transport direction for the deformed $N = 10$ ribbon on two electrodes (Fig. S2). Locations of Mo layers at two edges (layers 1,2 and 9,10) are labeled in the figure. Significantly lower electrostatic potentials at edge layers can be seen in the figure. Similar effects of deformation on band structure are found for other ribbons with different widths (see Fig. S3 in SI). In Table S1 in SI, we list the calculated deformation-caused bandgap drops for MoS_2 nanoribbons with various widths (from $N = 10$ to $N = 18$). In all cases, the bandgap drop is quite significant ranging from 0.27 eV (for $N = 18$) to 0.41 eV (for $N = 14$).

3.4 Transport properties of the Au(111)/MoS$_2$/Au(111) device

Here we study how the deformation-caused electronic structure changes affect transport properties of MoS_2 nanoribbons. For this purpose, we set up an Au/MoS_2/Au device made of two Au(111) electrodes and a middle $N = 10$ MoS_2 nanoribbon. We consider both cases of flat (Fig. 1c) and deformed (Fig. 3) ribbons. Note that the source is on the left and the drain is on the right. In Fig. 5(a), the calculated projected density of states (PDOS) of MoS_2 adsorbed on two Au(111) electrodes in the Au/MoS_2/Au junction is shown. The upper panel is for the case of flat ribbon and the lower panel for the one with structure deformation. By comparing wave functions at PDOS peaks with those of isolated ribbons, conduction bands (C) and valence bands (V) are identified in the plots. Due to the coupling with Au electrodes, both systems are metallic as there are no clear gaps in PDOS spectra. The charge transfer from Au to the ribbon shifts the Fermi energy significantly towards the
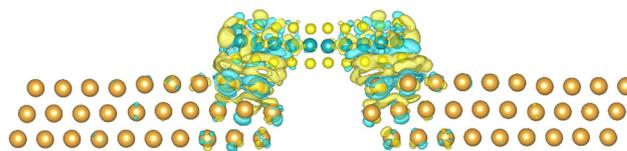

Fig. 2 Energy variation during the structure optimization process. The spontaneous deformation of the MoS_2 nanoribbon can be clearly seen. The definition of the curvature κ is also indicated.

Fig. 3 The iso-surface of calculated differential charge density: $\Delta\rho = \rho_{system} - \rho_{MoS_2} - \rho_{Au}$. Yellow (blue) represents electron accumulation (depletion).

This journal is © The Royal Society of Chemistry 2026

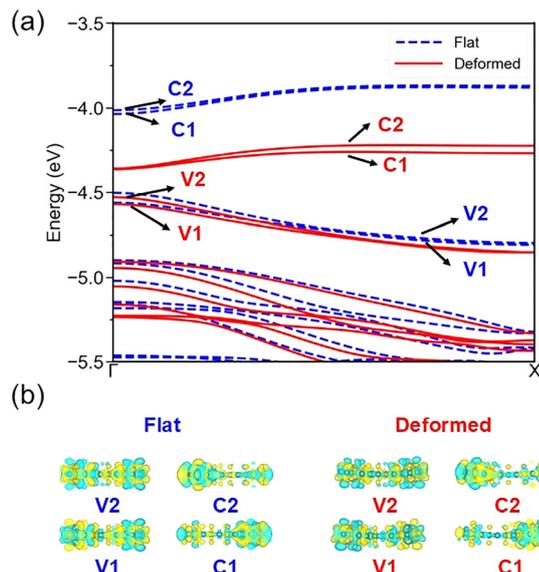*J. Mater. Chem. C*, 2026, **14**, 7641–7647 | **7643**

Fig. 4 (a) Band structures of the isolated flat (blue dashed line) and deformed (red solid line) MoS$_2$ nanoribbons with $N = 10$. C1, C2 and V1, V2 are two nearly degenerate conduction and valence bands, respectively. (b) Calculated wave functions of conduction and valence bands (at gamma point) of the isolated flat and deformed MoS$_2$ nanoribbons.

conduction bands for both cases, and the deformed ribbon shows a narrower separation between conduction and valence peaks than the flat one by about 0.22 eV, consistent with the trend observed in band structures.

We then calculate the current–voltage (I–V) characteristics of the Au/MoS$_2$/Au device for both flat and deformed ribbons. The results are shown in Fig. 5b, which indicates that the structure deformation significantly improves the conductivity of the $N = 10$ MoS$_2$ nanoribbon. At 0.5 V, the electric current starts to increase rapidly for the deformed ribbon. At 0.7 V, the electric current is around 215 nA for the deformed ribbon and 66 nA for the flat one.

To understand transport properties of the device, we calculate the transmission spectrum under various bias voltages for both the flat (Fig. 6a) and the deformed (Fig. 6b) ribbons. Under 0 V, the tunneling through two degenerate conducting edge states yields a transmission peak (peak C) around the Fermi energy (0 eV in two figures) for both cases. The center of the peak C is slightly above (below) the Fermi energy for the flat (deformed) ribbon, which is consistent with the PDOS shown in Fig. 5a. When the bias is nonzero, the degeneracy of two edge states is lifted. When the bias increases, transmission peaks of two edge states, C_1 and C_2, move with the Fermi energies of the drain (on the right) and the source (on the left), respectively. For both ribbons, two transmission peaks are suppressed by the bias voltage, as shown in Fig. 6a and b. For the flat ribbon, the C_1 peak almost disappears (falling below the numerical accuracy limit). In contrast, for the deformed ribbon, the C_1 peak shifts into the bias window at 0.5 V, markedly enhancing the current relative to the flat case. Iso-surface plots for tunneling eigenchannels at peaks C_1 and C_2 for the deformed ribbon under 0.5 V (Fig. 6c and d) clearly show that the two peaks are caused by tunneling through two edge states of the $N = 10$ ribbon (see two edge states in Fig. 4b).

The transport properties of localized edge states would be sensitively dependent on the width of the ribbon. Indeed, our transport calculations for the deformed ribbon with $N = 12$, 14, 16 and 18 show that the conductivity of these ribbons at lower biases (<0.6 V) are essentially the same and significantly lower than that of $N = 10$ one (Fig. 7a). In PDOS and transmission spectrum for $N = 12$ ribbon (Fig. 7b), we see that the edge states, C and V, are all insulating. The inset in Fig. 7b (lower panel) shows iso-surfaces of localized states (C and V), in which we see that $N = 12$ ribbon is wide enough to completely separate two edge states, causing low conductance of the ribbon. We also show the calculated PDOS and transmission function for $N = 18$ ribbon in Fig. S4 in SI, for which similar trends as those of $N = 12$ can be seen.
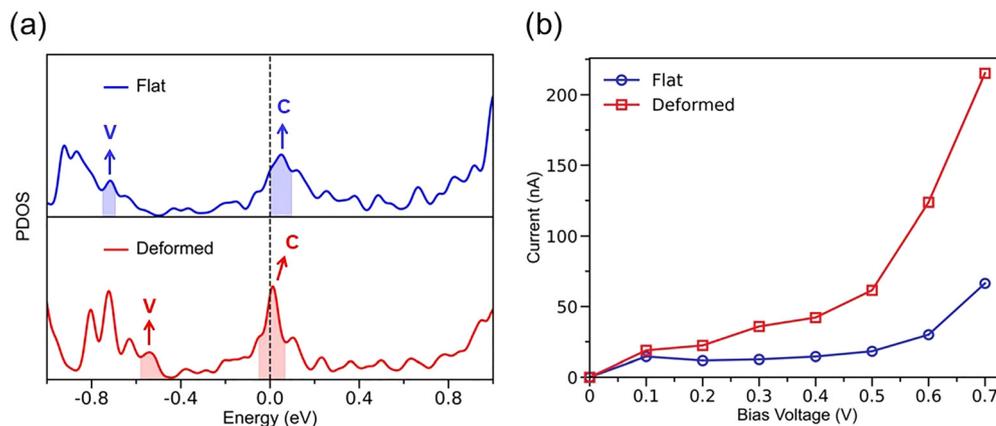

Fig. 5 (a) Calculated PDOS for the flat MoS$_2$ nanoribbon (upper) and the deformed ribbon when MoS$_2$ nanoribbons are adsorbed on two Au(111) electrodes. Conduction (valence) peaks are denoted by C (V). The Fermi level of both systems is set to 0.0 eV. (b) Calculated I–V characteristics for Au/MoS$_2$/Au devices with a flat and deformed MoS$_2$ nanoribbon.

7644 | *J. Mater. Chem. C*, 2026, **14**, 7641–7647

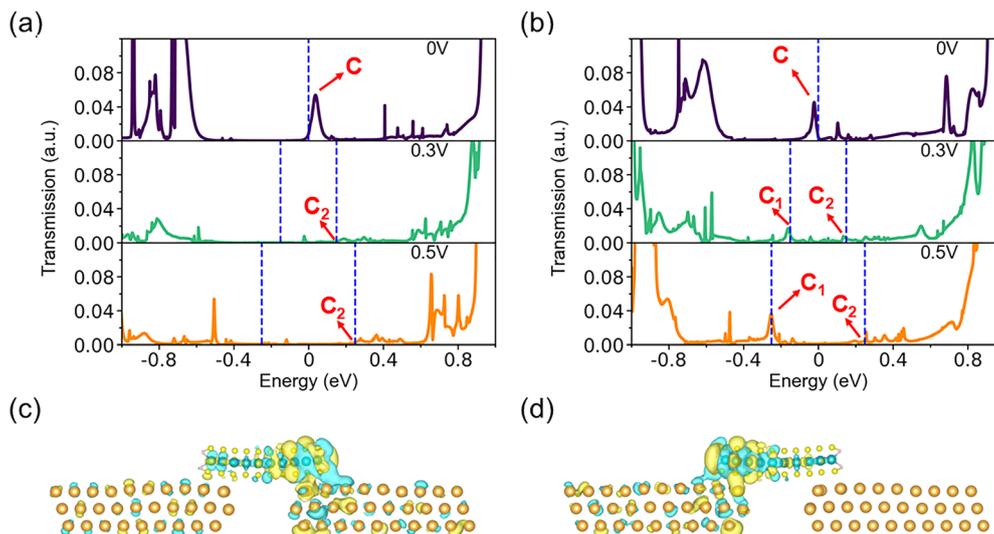This journal is © The Royal Society of Chemistry 2026

Fig. 6 (a) Transmission spectra of the system with a flat MoS$_2$ nanoribbon (N = 10) at bias voltages of 0, 0.3, and 0.5 V. The blue dashed lines indicate the bias window. (b) Transmission spectra of the system with a deformed MoS$_2$ nanoribbon (N = 10) at 0, 0.3, and 0.5 V. Peaks C1 and C2 originate from tunneling through edge states localized on the right (drain) and left (source) contacts, respectively. Tunneling eigenchannels at peaks C$_1$ and C$_2$ for the deformed ribbon under 0.5 V are shown in (c) and (d) respectively.
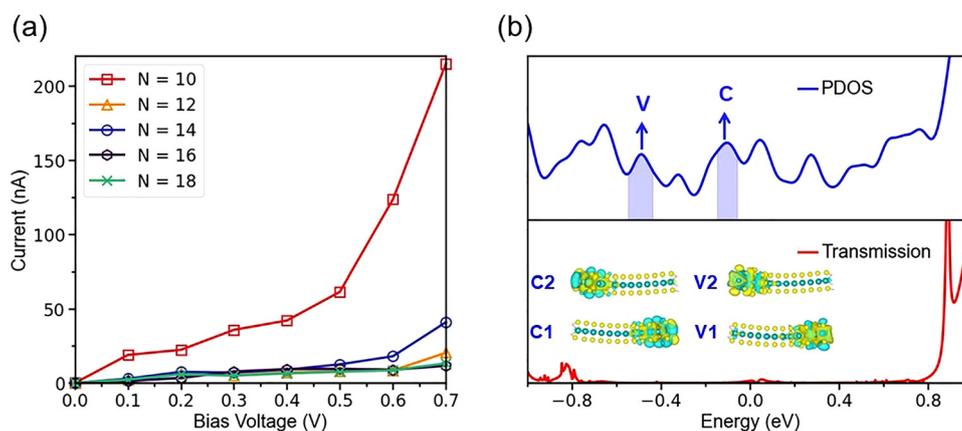

Fig. 7 (a) I–V characteristics of different widths of the MoS$_2$ nanoribbon within the Au/MoS$_2$/Au devices. The bias voltage is applied between two Au electrodes. (b) PDOS and transmission spectrum for the deformed MoS$_2$ nanoribbon with N = 12. The blue line represents the PDOS, while the red line represents the transmission. Peaks C and V correspond to states primarily originating from the conduction and valence bands of the MoS$_2$ nanoribbon, respectively. The wavefunctions C1 and C2 correspond to the degenerate conduction bands, while V1 and V2 correspond to the degenerate valence bands of the MoS$_2$ nanoribbon.

4. Conclusions

In conclusion, by first-principles calculations, we show that MoS$_2$ nanoribbons adsorbed on two Au(111) electrodes in an Au/MoS$_2$/Au junction undergo spontaneous structural deformation involving bending and stretching. The deformation lowers the energies of conduction bands formed by localized edge states, leading to significant decrease of band gaps of the ribbons. For narrow ribbons (N =10), in which the edge states are conducting, we find that the spontaneous deformation greatly enhances the conductivity of the ribbon. For longer ribbons ($N \geq 12$), the deformation shows little effects on transport properties. These studies enhance our understanding of the structural and electronic properties of MoS$_2$ nanoribbons on metal electrodes within device configurations, providing valuable insights for the future development of MoS$_2$-based electronic devices.

Conflicts of interest

There are no conflicts to declare.

Data availability

The data supporting this article have been included as part of the supporting information (SI). Supporting information: Fig.

This journal is © The Royal Society of Chemistry 2026

J. Mater. Chem. C, 2026, **14**, 7641–7647 | **7645**

S1, band structures of MoS_2 ribbon and bulk Au from SIESTA and VASP calculations; Fig. S2, Planar-averaged electrostatic potential V(z) along the transport direction for the deformed MoS_2 nanoribbon device; Tables S1, effective curvature, curvature radius, stretching, and deformation induced bandgap drops of nanoribbons with different width; Fig. S3, band structures of isolated MoS_2 ribbons with different width; Fig. S4, PDOS and transmission spectrum for the deformed MoS_2 nanoribbon with N = 18. See DOI: https://doi.org/10.1039/d6tc00052e.

All structural and energy calculations were done with widely used commercialized VASP (version 5.4) and free SIESTA (version 5.1) computational packages. The nonequilibrium transport calculations were done with our homemade code SS-DFT that has been widely used for studying transport properties of nanoscale junctions. References for these computational packages can be found in the main text.

Acknowledgements

References

1 C. Liu, H. Chen, S. Wang, Q. Liu, Y. G. Jiang, D. W. Zhang, M. Liu and P. Zhou, Two-dimensional materials for next-generation computing technologies, *Nat. Nanotechnol.*, 2020, **15**, 545–557.

2 Y. Liu, X. Duan, H. J. Shin, S. Park, Y. Huang and X. Duan, Promises and prospects of two-dimensional transistors, *Nature*, 2021, **591**, 43–53.

3 K. S. Kim, J. Kwon, H. Ryu, C. Kim, H. Kim, E. K. Lee, D. Lee, S. Seo, N. M. Han, J. M. Suh and J. Kim, The future of two-dimensional semiconductors beyond Moore's law, *Nat. Nanotechnol.*, 2024, **19**, 895–906.

4 S. Das, A. Sebastian, E. Pop, C. J. McClellan, A. D. Franklin, T. Grasser, T. Knobloch, Y. Illarionov, A. V. Penumatcha, J. Appenzeller and Z. Chen, Transistors based on two-dimensional materials for future integrated circuits, *Nat. Electron.*, 2021, **4**, 786–799.

5 F. Wu, H. Tian, Y. Shen, Z. Hou, J. Ren, G. Gou, Y. Sun, Y. Yang and T.-L. Ren, Vertical MoS_2 transistors with sub-1-nm gate lengths, *Nature*, 2022, **603**, 259–264.

6 Q. Hua, G. Gao, C. Jiang, J. Yu, J. Sun, T. Zhang, B. Gao, W. Cheng, R. Liang, H. Qian and W. Hu, Atomic threshold-switching enabled MoS_2 transistors towards ultralow-power electronics, *Nat. Commun.*, 2020, **11**, 6207.

7 S. Hwangbo, L. Hu, A. T. Hoang, J. Y. Choi and J. H. Ahn, Wafer-scale monolithic integration of full-colour micro-LED display using MoS_2 transistor, *Nat. Nanotechnol.*, 2022, **17**, 500–506.

8 J. Daniel, Z. Sun and X. Zhang, *et al.*, Experimental demonstration of an on-chip p-bit core based on stochastic magnetic tunnel junctions and 2D MoS_2 transistors, *Nat. Commun.*, 2024, **15**, 4098.

9 B. Radisavljevic, A. Radenovic, J. Brivio, V. Giacometti and A. Kis, Single-layer MoS_2 transistors, *Nat. Nanotechnol.*, 2011, **6**, 147–150.

10 K. F. Mak, C. Lee, J. Hone, J. Shan and T. F. Heinz, Atomically thin MoS_2: a new direct-gap semiconductor, *Phys. Rev. Lett.*, 2010, **105**, 136805.

11 A. T. Hoang, L. Hu, B. J. Kim, T. T. N. Van, K. D. Park, Y. Jeong, K. Lee, S. Ji, J. Hong, A. K. Katiyar and B. Shong, Low-temperature growth of MoS_2 on polymer and thin glass substrates for flexible electronics, *Nat. Nanotechnol.*, 2023, **18**, 1439–1447.

12 J. Park, H. S. Im, J. H. Park, J. Kim, D. Yoo, H. Jang, D. H. Kang, J. K. Shin, H. Kim, Y. S. Kim, J. Lee and W. J. Yoo, Mechanically reliable and electronically uniform monolayer MoS_2 by passivation and defect healing, *Nature*, 2023, **616**, 280–285.

13 D. Lembke and A. Kis, Breakdown of high-performance monolayer MoS_2 transistors, *ACS Nano*, 2012, **6**, 10070–10075.

14 A. Nourbakhsh, A. Zubair, R. N. Sajjad, A. K. G. Tavakkoli, W. Chen, S. Fang, X. Ling, J. Kong, M. S. Dresselhaus, E. Kaxiras, K. K. Berggren, D. Antoniadis and T. Palacios, MoS_2 field-effect transistor with sub-10 nm channel length, *Nano Lett.*, 2016, **16**, 7798–7806.

15 R. Ge, X. Wu, M. Kim, J. Shi, S. Sonde, L. Tao, Y. Zhang, J. C. Lee and D. Akinwande, Atomristor: nonvolatile resistance switching in atomic sheets of transition metal dichalcogenides, *Nano Lett.*, 2018, **18**, 434–441.

16 H. K. Ng, D. Xiang, A. Suwardi, G. Hu, K. Yang, Y. Zhao, T. Liu, Z. Cao, H. Liu, S. Li, J. Cao, Q. Zhu, Z. Dong, C. K. I. Tan, D. Chi, C.-W. Qiu, K. Hippalgaonkar, G. Eda, M. Yang and J. Wu, Improving carrier mobility in two-dimensional semiconductors with rippled materials, *Nat. Electron.*, 2022, **5**, 489–496.

17 T. Liu, S. Liu, K.-H. Tu, H. Schmidt, L. Chu, D. Xiang, J. Martin, G. Eda, C. A. Ross and S. Garaj, Crested two-dimensional transistors, *Nat. Nanotechnol.*, 2019, **14**, 223–226.

18 L. Yu, A. Ruzsinszky and J. P. Perdew, Bending two-dimensional materials to control charge localization and Fermi-level shift, *Nano Lett.*, 2016, **16**, 2444–2449.

19 N. K. Nepal, L. Yu, Q. Yan and A. Ruzsinszky, First-principles study of mechanical and electronic properties of bent monolayer transition metal dichalcogenides, *Phys. Rev. Mater.*, 2019, **3**, 073601.

20 H. Tang, B. Neupane, S. Neupane, S. Ruan, N. K. Nepal and A. Ruzsinszky, Tunable band gaps and optical absorption properties of bent MoS_2 nanoribbons, *Sci. Rep.*, 2022, **12**, 3008.

21 E. Artacho, D. Sánchez-Portal, P. Ordejón, A. García and J. M. Soler, Linear-scaling ab-initio calculations for large and complex systems, *Phys. Status Solidi B*, 1999, **215**, 809–817.

7646 | *J. Mater. Chem. C*, 2026, **14**, 7641–7647

This journal is © The Royal Society of Chemistry 2026

22 J. M. Soler, E. Artacho, J. D. Gale, A. García, J. Junquera, P. Ordejón and D. Sánchez-Portal, The SIESTA method for ab initio order-N materials simulation, *J. Phys.: Condens. Matter*, 2002, **14**, 2745–2779.

23 E. Artacho, E. Anglada, O. Diéguez, J. D. Gale, A. García, J. Junquera, R. M. Martin, P. Ordejón, J. M. Pruneda, D. Sánchez-Portal and J. M. Soler, The SIESTA method; developments and applicability, *J. Phys.: Condens. Matter*, 2008, **20**, 064208.

24 S. Liu, A. Nurbawono and C. Zhang, Density functional theory for steady-state nonequilibrium molecular junctions, *Sci. Rep.*, 2015, **5**, 15386.

25 H. Wang, K. M. Yam, Z. Jiang, N. Guo and C. Zhang, Structure phase change induced by nonequilibrium effects in molecular-scale junctions, *Phys. Rev. B*, 2024, **110**, L121405.

26 J. P. Perdew, K. Burke and M. Ernzerhof, Generalized gradient approximation made simple, *Phys. Rev. Lett.*, 1996, **77**, 3865–3868.

27 N. Troullier and J. L. Martins, Efficient pseudopotentials for plane-wave calculations, *Phys. Rev. B: Condens. Matter Mater. Phys.*, 1991, **43**, 1993–2006.

28 S. Liu, Y. P. Feng and C. Zhang, Communication: Electronic and transport properties of molecular junctions under a finite bias: A dual mean field approach, *J. Chem. Phys.*, 2013, **139**, 194106.

29 Z. Jiang, K. M. Yam, N. Guo, L. Zhang, L. Shen and C. Zhang, Prominent nonequilibrium effects beyond the standard first-principles approach in nanoscale electronic devices, *Nanoscale Horiz.*, 2021, **6**, 801–808.

30 G. Kresse and J. Furthmüller, Efficiency of ab-initio total energy calculations for metals and semiconductors using a plane-wave basis set, *Phys. Rev. B: Condens. Matter Mater. Phys.*, 1996, **54**, 11169–11186.

31 P. E. Blöchl, Projector augmented-wave method, *Phys. Rev. B: Condens. Matter Mater. Phys.*, 1994, **50**, 17953.

32 P. Johari and V. B. Shenoy, Tuning the electronic properties of semiconducting transition metal dichalcogenides by applying mechanical strains, *ACS Nano*, 2012, **6**, 5449–5456.

33 G. Boschetto, S. Carapezzi, C. Delacour, M. Abernot, T. Gil and A. Todri-Sanial, Ab Initio Computer Simulations on Interfacial Properties of Single-Layer MoS_2 and Au Contacts for Two-Dimensional Nanodevices, *ACS Appl. Nano Mater.*, 2022, **5**, 10192–10202.

34 S. Grimme, S. Ehrlich and L. Goerigk, Effect of the damping function in dispersion corrected density functional theory, *J. Comput. Chem.*, 2011, **32**, 1456–1465.

35 Y. Wang and H. Cheng, First-principles simulations of a graphene-based field-effect transistor, *Phys. Rev. B: Condens. Matter Mater. Phys.*, 2015, **91**, 245307.

This journal is © The Royal Society of Chemistry 2026

J. Mater. Chem. C, 2026, **14**, 7641–7647 | 7647